Micron 121 (2019) 8–20

Contents lists available at ScienceDirect

Micron

journal homepage: www.elsevier.com/locate/micron

Electron beam damage of perfluorosulfonic acid studied by soft X-ray spectromicroscopy

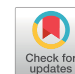

Lis G.A. Melo*, Adam P. Hitchcock

Dept. Chemistry and Chemical Biology, McMaster University, Hamilton, ON, L8S4M1, Canada

ARTICLE INFO

Keywords:
Transmission electron microscope
Soft materials
Radiation damage
STXM
Electron beam damage
Perfluorosulfonic acid

ABSTRACT

Scanning transmission X-ray microscopy (STXM) was used to study chemical changes to perfluorosulfonic acid (PFSA) spun cast thin films as a function of dose imparted by exposure of a 200 kV electron beam in a Transmission Electron Microscope (TEM). The relationship between electron beam fluence and absorbed dose was calibrated using a modified version of a protocol based on the positive to negative lithography transition in PMMA [Leontowich et al, J. Synchrotron Rad. 19 (2012) 976]. STXM was used to characterize and quantify the chemical changes caused by electron irradiation of PFSA under several different conditions. The critical dose for CF_2-CF_2 amorphization was used to explore the effects of the sample environment on electron beam damage. Use of a silicon nitride substrate was found to increase the CF_2-CF_2 amorphization critical dose by ~x2 from that for free-standing PFSA films. Freestanding PFSA and PMMA films were damaged by 200 kV electrons at ~100 K and then the damage was measured by STXM at 300 K (RT). The lithography cross-over dose for PMMA was found to be ~2x higher when the PMMA thin film was electron irradiated at 120 K rather than at 300 K. The critical dose for CF_2-CF_2 amorphization in PFSA irradiated at 120 K followed by warming and delayed measurement by STXM at 300 K was found to be ~2x larger than at 300 K. To place these results in the context of the use of electron microscopy to study PFSA ionomer in fuel cell systems, an exposure of 300 e^-/nm^2 at 300 K (which corresponds to an absorbed dose of ~20 MGy) amorphizes ~10% of the CF_2-CF_2 bonds in PFSA. At this dose level, the spatial resolution for TEM imaging of PFSA is limited to 3.5 nm by radiation damage, if one is using a direct electron detector with DQE = 1. This work recommends caution about 2D and 3D morphological information of PFSA materials based on TEM studies which use fluences higher than 300 e^-/nm^2.

1. Introduction

Optimization of spatial distributions of perfluorosulfonic acid (PFSA) is a key target to improve performance and minimize costs in polymer electrolyte membrane fuel cells (PEMFC). Understanding the structure of the hydrophilic channels in hydrated PFSA can help model the transport of protons in the membrane. Quantitative mapping of PFSA in the cathode (where it is usually called ionomer) is needed to improve efficiency by optimizing the spatial distribution of ionomer in the cathode, allowing a reduction in amount of catalyst and thus cost. X-ray scattering techniques have given considerable insight into the nanoscale morphology of PFSA (Kusoglu and Weber, 2017). However, several different models can explain the scattering data equally well, leading to ambiguity. Direct visualization of the nanostructure of dry and hydrated PFSA with sub-nm spatial resolution has been attempted several times using (scanning) transmission electron microscopy, (S)TEM (Allen et al., 2015; Peron et al., 2010; Wang et al., 2013). However, a major concern for electron microscopy when applied to radiation sensitive materials such as PFSA is that radiation damage limits the achievable spatial resolution (Egerton, 2012; Egerton et al., 2012) and can result in damage artifacts such as mass loss and/or chemical changes (Yakovlev et al., 2013). Recently, Yakovlev et al., 2013 claimed that "*morphologies that have been observed (in the literature) are, in many cases, artifacts caused by (radiation) damage.*"

The objective of this work is to study and quantify the chemical changes caused by electron beam irradiation in PFSA in order to address the following questions: *How does PFSA damage as a function of electron exposure (dose)? By how much does the use of cryo temperature influence the damage of PFSA? Is it possible to acquire high resolution TEM images to map the morphology of the phase-segregated hydrophilic and hydrophobic channels without distortion by radiation damage?* Here, we assume that the highest quality quantitative analysis of PFSA is done with minimal (ideally, no) modification to its chemical or physical structure. Imaging of heavily damaged material can be useful in some

* Corresponding author.
E-mail address: lismellow@gmail.com (L.G.A. Melo).

https://doi.org/10.1016/j.micron.2019.02.006
Received 30 November 2018; Received in revised form 8 February 2019; Accepted 19 February 2019
Available online 07 March 2019
0968-4328/ Crown Copyright © 2019 Published by Elsevier Ltd. All rights reserved.

circumstances, but this is not the situation addressed in this paper.

Scanning Transmission X-ray Microscopy using near edge X-ray absorption (NEXAFS) contrast is analogous to (S)TEM combined with Electron Energy Loss Spectroscopy (EELS). The main advantage of STXM-NEXAFS for the analysis of soft materials like PFSA is that the dose needed to obtain a given amount of analytical information is much smaller than that needed in TEM-EELS (Braun et al., 2005; Hitchcock et al., 2008; Rightor et al., 1997; Wang et al., 2009a). STXM has been used to study the radiation damage chemistry of several soft materials, including: polystyrene damaged by soft X-rays (Coffey et al., 2002; Wang et al., 2009b) and ultraviolet radiation (Klein et al., 2008); poly (methyl methacrylate, PMMA) damaged by soft X-rays (Beetz and Jacobsen, 2003; Leontowich, 2012; Leontowich et al., 2012; Wang et al., 2009b; Zhang et al., 1995); polyethylene terephthalate damaged by soft X-rays and electrons (Rightor et al., 1997; Wang et al., 2009a); biological materials damaged by soft X-rays (Bedolla et al., 2018; Cody et al., 2009; Gianoncelli et al., 2015; Wang et al., 2009b; Zubavichus et al., 2004); as well as several other polymers damaged by soft X-rays (Coffey et al., 2002; Leontowich, 2013; Leontowich et al., 2016; Wang, 2008) and ion beams (Bassim et al., 2012; Bernard et al., 2009; Melo et al., 2016). A summary of the species studied, critical doses and other aspects of radiation damage studied by STXM is given in the supplemental information, Table S-1.

Ultra-low exposure imaging is considered 800 e^-/nm^2 in electron tomography for a complete tilt series acquisition (Migunov et al., 2015), or 500 e^-/nm^2 in atomic resolution imaging of biological materials using direct electron detectors (Rodriguez et al., 2017) and 160 e^-/nm^2 for liquid sample imaging (Kammeyer et al., 2017). Much larger exposures / doses are required for analytical measurements by TEM-EELS or energy dispersive spectroscopy (TEM-EDS) (Cullen et al., 2014; Melo et al., 2017). An exposure of ~30,000 e^-/nm^2 at 300 K (room temperature, RT) is needed for quantifying fluorine in PFSA films with adequate signal to noise ratio using a high efficiency solid state X-ray detector (FEI Super X). At this exposure, there is extensive mass loss and chemical damage to PFSA (Melo et al., 2017). The exposure needed for adequate signal to noise is lower in TEM-EDS systems with larger area detectors but radiation damage is still a major limitation (Ovsyanko et al., 2018). Exposure (also called fluence) is commonly used in the TEM community as a measure of dose since it is proportional to the dose (energy deposited per mass of sample) except for thick specimens. However, there is a difference between exposure (also called fluence), which is the time- integrated areal density of electrons incident on the surface of a sample) and dose, which is the energy absorbed per unit mass of the sample. In this work, we have used dose rather than exposure since it is the correct measure of the radiation damage inducing agent.

This work reports STXM characterization of the damage chemistry and measurement of critical doses for radiation damage to PFSA by 200 kV electron irradiation in a TEM. First, the relationship of the electron beam exposure (fluence in e^-/nm^2) to the delivered dose (in MGy) was calibrated by exposing PMMA under controlled conditions, chemically developing the films, and calibrating the dose with the positive to negative lithography cross-over. This method was developed and documented previously, and used to determine the efficiency of X-ray microscope detectors (Leontowich et al., 2012). A modification of the method was used, as outlined in the experimental section. Then, spun cast PFSA films were damaged with 200 kV electrons in a TEM under a range of doses and post-damage analysis was done with room-temperature STXM. The effect of sample temperature on damage kinetics was studied by electron beam irradiation with the sample both at ambient temperature (RT, 300 K) and under cryo conditions (100 or 120 K) using a cryogenic sample mount. Critical doses were evaluated for changes to specific spectroscopic features and to the extent of elemental loss. The critical dose values for samples mounted on Cu grids without any substrate were compared to those for samples mounted on a silicon nitride (SiNx) membrane substrate. The chemical changes and critical doses for damage by 200 kV electrons and soft X-rays are compared. Both electrons and X-rays result in similar damage chemistry, which is dominated by -(CF_2-CF_2)- amorphization (structural disorder) and fluorine loss. Our post-damage STXM analysis indicates that the critical doses for both mass loss and CF_2-CF_2 amorphization of PFSA by 200 kV electrons are ~2x larger when the sample is damaged at 100 K rather than at RT. Some of these results have been presented previously as a conference proceeding (Melo and Hitchcook, 2018a).

2. Experimental methods

2.1. Sample preparation

Dupont-D521 5 wt% alcohol-based dispersed ionomer solutions with equivalent weight[1] of 1100 (Ion Power Inc.) were diluted to 2 and 4 wt% solutions with isopropanol (99.5%, Caledon Laboratory Chemicals) to achieve the desired film thickness. 1.5% w/w solutions of PMMA (molecular weight of 120000, Polymer source, GPC MKBB7676) were prepared in toluene 99.9% (Chromasolv). Ultrasonication was used to ensure the solutions were dispersed (5 min. for each). The solutions were spin coated (6708D, Specialty Coating Systems) on cleaved mica surfaces (Ted Pella) using 4500 rpm for 30 s at ambient temperature and pressure. A clean razor blade was used to gently cut ~1 mm^2 squares on the top surface of the film. The spun cast films were transferred to a TEM grid or silicon nitride (SiNx) window by first floating the film on to the surface of distilled water by inserting each individual mica piece at ~45° angle. Prior to floating, the water surface was cleaned of particulates by passing a lens paper over it. The film was then transferred from the water surface to TEM SiNx windows (100 or 500 µm square windows of 20, 50 or 100 nm thick silicon nitride membranes, in 3 mm diameter, 100 and 200 µm thick Si frames, from Silson Ltd (SiRN-TEM-200-0.5-100) and SiMPore SiN_x TEM grids or TEM Cu finder grids (200 mesh) (Electron Microscopy Sciences, G200F2-Cu). The transfer was performed under an optical microscope using an eye-lash waxed to a wooden stick to orient the films on the interface of the water surface prior to pick-up onto the window or grid. Multiple films of the same sample were deposited on each SiNx window. One sample was prepared at a time, and the water bath was changed after each sample. The films were always deposited on the grid or windows with empty areas nearby, in order to have suitable areas for incident flux (I_o) determination in subsequent STXM measurements. The PMMA films spun cast from 1.5 wt% solutions are 46 ± 4 nm thick as measured with STXM and Ultraviolet Spectral Reflectance (Melo, 2018; Melo et al., 2018).

2.2. TEM damage

Prior to electron beam exposure, transmission and reflection mode optical microscopy images of all samples were recorded using 5x (numerical apertures, NA, = 0.15) or 20x (NA = 0.30) objective lenses. Areas of interest were identified beforehand to avoid unnecessary damage from navigation in the TEM. All electron beam exposures were done using full field transmission mode in a JEOL model 2010 F microscope with a field emission electron gun (FEG) operated at 200 kV in the Canadian Centre for Electron Microscopy at McMaster University. A Gatan model 4-950-90 cryo-holder was used, and a temperature of 120 K was used for the PMMA study while a temperature of 100 K was used for the PFSA study.

Several specimens of PFSA and PMMA materials were damaged for a range of controlled doses. The orientation of the grid/window and the areas of interest were identified using low magnification. When changing magnification, there is potential confusion from rotation of the

[1] Equivalent weight is defined as the weight of the dry material in acid form per mole of sulfonic acid group (Mauritz and Moore, 2004).

Table 1
Parameters used for 200 kV electron irradiation of PMMA and PFSA films using transmission mode in a JEOL-2010 F.

Sample	Temperature (K)	Current (pA)[a]	Exposure time (s)	Electron Fluence (e^-/nm^2)	Fluence rate ($e^-/nm^2/s$)
PMMA/SiNx	RT	50–60	2–120	125–8000	60, 63 & 147
PMMA/SiNx	120	120–150	5–70	700–12000	63 & 168
PFSA	100	53–55	2–60	200–6300	105, 109, 313 & 573
PFSA	RT	54	2–16	200–1800	107–429
PFSA /SiNx	RT	50–56	2–180	200–50000	100–445

[a] The current indicated in this column is 10x the value reported by the instrument, based on a direct calibration using a Faraday cup.

image which results in additional exposure. This was minimized by working at the edge of a Cu grid square or beside the frame of the SiNx window.

Table 1 summarizes all electron irradiation conditions used in this work. The beam energy was 200 kV while the HT dark current and emission currents of the FEG gun were 114 μA and 172 μA, respectively. Table 1 also indicates the fluence rate, which may play a role in determining the extent of damage. We used only a small range of fluence rates, and did not examine its effect systematically, and thus leave the issue of a possible damage rate effect to a future study.

Damage spots were made by restricting the beam so that only the 2 cm diameter fluorescent screen, which measures current, was illuminated. The beam size was adjusted so that it just illuminated the 2 cm diameter screen - see the schematic shown in Figure S-1. The exposure area on the sample (A_s) observed in the post-damage STXM images are related to the magnification by an inverse square relationship according to:

$$A_s = \pi\left(\frac{2r}{10^7 M}\right)^2 \quad (1)$$

where M is the magnification used during damage of the JEOL microscope, r is the radius of the small fluorescent screen (1.0 cm) and A_s is given in nm^2. The current reported by the microscope was low by $\times 10$, as verified with current measurements using a Faraday cup. Exposure times were varied from 2 s to 2 min. The exposure time was controlled by manually clicking a button that inserts or removes the shutter. Two seconds is the lowest practical controlled exposure time due to delays while opening and closing the shutter. The fluence (F) in e^-/nm^2 was calculated by:

$$F = \frac{i \cdot t}{1.6 \cdot 10^{-19} \cdot A_s} \quad (2)$$

where i is the current of the incident electrons (units in A, only illuminating the 2 cm screen), t is the exposure time (s) and A_s is in nm^2.

After the cryo-TEM sessions were completed, the cooled samples were warmed up to RT. The damaged regions of all samples were imaged optically in reflection mode using 50x (NA = 0.75) or 100x (NA = 1.25) objective lens. The PFSA samples were taken to STXM microscopes for detailed analysis, usually after several days or a week delay. All samples used in this work, and the conditions of irradiation are listed in Table 2.

2.3. PMMA development and electron dose determination - method

Depending on the dose applied, PMMA can act as either a positive and negative resist (Zailer et al., 1996). After electron irradiation, the exposed PMMA films (still on its SiNx or TEM grid support) were held in locking tweezers and developed by gently swirling in a glass vial containing a 3:1 v/v solution of isopropanol (IPA) and 4-methyl-2-pentanone (MIBK) for 4 s at room temperature. The films were then washed for 4 s in a separate IPA solution. These development and washing times are much shorter than those reported previously (Leontowich et al., 2012) probably because the molecular weight of the PMMA used in this work was much lower (120 kD compared to 315 kD). After development, the films were air-dried and optical microscopy images were taken of all damaged areas to identify the positive to negative crossover. The chemical development removes the non-cross-linked, low dose irradiated material to a greater extent than the unexposed polymer, resulting in less material in the areas that were exposed to the ionizing beam after development (positive mode). The areas that were exposed to high doses are cross-linked and insoluble irradiated material (negative mode).

In the original work which developed the lithography positive to negative mode transition as a tool to quantify dose, the cross-over transition was reported to occur at 90 ± 4 MGy (Leontowich et al., 2012). We have recently published a first principles approach for determining the absorbed dose in X-ray absorption (Berejnov et al., 2018). The absorbed dose depends on the material and the type of radiation damage that occurs. In materials which suffer mass loss, which is the case for both PMMA and PFSA, it was demonstrated that the decrease of mass with increasing dose can be disregarded for the calculation of the absorbed dose (Berejnov et al., 2018) since the change in absorption (and thus deposited energy) and the change in the mass present in the irradiated area decrease proportionately, such that the dose (energy/mass) is independent of the extent of mass loss, to first approximation. In the derivation of the lithography cross-over dose for PMMA in Leontowich et al. (2012) an incorrect expression for dose in the case of mass loss, which was first reported in Wang et al., 2009b, was used which underestimated the X-ray absorbed dose (see Berejnov et al., 2018 for details). The dose for the lithography transition of PMMA based on the correct treatment, which ignores mass loss, is 104 ± 4 MGy. After the chemical development, pads that received a dose larger than 104 MGy are thicker than the rest of the film (negative mode). Pads that receive a dose less than 104 MGy are dissolved and are thinner than the surrounding material (or in this case, completely dissolved; positive mode). The visible pad that had the least dose identifies the lowest exposure above 104 MGy, while the pad at the next lower dose is that below the lithography transition. We calibrated the exposure–dose relationship by assigning the exposure half way between the exposures for these two pads to 104 MGy.

2.4. PMMA development and electron dose determination - experimental

Fig. 1 shows an example of how the fluence - dose calibration was performed using the positive to negative cross-over in PMMA. Optical images (reflection, 50x objective, reflection mode) of a damage series in PMMA deposited on a SiNx window (sample set A, Table 2) are shown before (Fig. 1a) and after development (Fig. 1b). Line profiles of the damage series in Fig. 1a and b are shown in Fig. 1c. Areas that received doses < 50 MGy are not visible with optical microscopy either before or after development. Areas that received doses from 50 to 100 MGy are visible before development, but are barely visible after development. Only areas that received doses higher than ~104 MGy, where the PMMA is highly cross-linked and thus has much lower solubility than the surrounding undamaged PMMA, are visible after development (Fig. 1b). The change from positive to negative mode occurred between spot 5 and spot 6 (1250 e^-/nm^2 and 1880 e^-/nm^2, respectively). This measurement was repeated in 10 areas in 4 different PMMA specimens made from the same solution. The fluence and calculated dose for the spots just before and just after the cross-over dose are listed in Table 3.

Table 2
Summary of data sets for STXM measurements of radiation damage in TEM and STXM.

Set	Sample (weight %)	Code	Run	Polymer Thickness (nm)	Substrate (Thickness, nm)	T (K)	Damage, enviro[a]	Analysis	Comment
A	PMMA 1.5%	LM066	–	50	SiNx (20)	RT	TEM	Optical	Fig. 1; Table 3
A1	PMMA 1.5%	LM062	–	50	none	RT	TEM	Optical	Fig. S2
A2	PMMA 1.5%	LM070	–	50	SiNx (20)	120	Cryo-TEM	Optical	Fig. 2; Table 3
A3	PMMA 1.5%	LM068	–	50	SiNx (20)	RT	TEM	Optical	Table 3
B	PFSA 2%	LM126	CLS-08/17	70-110	None	100	Cryo-TEM	C, O, F stacks	Fig. 3–9, S3 ‘Cryo-TEM pristine’
C	PFSA 2%	LM130	CLS-08/17	70-110	SiNx (70)	–	–	C, O, F stacks	Fig. S3; ‘X-ray pristine’
D	PFSA 2%	LM133	CLS-08/17	45-60	None	RT	TEM	C, F images	Fig. 7–9
E	PFSA 2%	LM129	CLS-08/17	95-110	SiNx (100)	RT	TEM	C, F images	Fig. 7–9
F	PFSA 2%	LM132	CLS-08/17	50-80	SiNx (100) + Pt (5)	RT	TEM	C, F images	Fig. 7–9
G	PFSA 3%	LM163	CLS-03/18	80-100	SiNx (70)	RT	STXM, He	C, F images	Fig. 8,9; STXM damage at 320 eV
H	PFSA 4%	LM030b	ALS-06/16	120	none	RT	STXM, He	C, F images	Fig. 8,9; STXM damage at 320 eV
I	PFSA 4%	LM058g	ALS-06/16	160-230	none	120	Cryo-TEM	C, F images	Fig. 9

[a] All samples damaged in the TEM were under similar vacum conditions, 10^{-5} Pa.

Based on the measured fluences before and after cross-over, the fluence corresponding to the dose of 104 MGy for the positive to negative crossover transition is 1.32 ± 0.18 × 10^3 e^-/nm^2 (uncertainty is the standard deviation).

Freestanding PMMA films were also intentionally damaged at RT. However, the areas could not sustain more than 650 e^-/nm^2, which corresponds to 50 MGy, before completely burning a hole. Figure S-2 (sample set A1, Table 2) shows a damage series in freestanding PMMA before development, where all areas result in the formation of holes in the films. The freestanding PMMA films did not survive development. One droplet of the development solution deposited on a grid held at 90° angle was sufficient to completely dissolve the film.

The fluences calculated using Eq. (2) were converted to dose using an average calibration factor of 0.079 MGy/(e^-/nm^2) derived from the average of the fluences for the pads just before and after the lithography cross-over measured from several damage series of several different PMMA samples. Table 3 summarizes results of the pre- and post-cross-over pad dose for 2 samples and 8 damage experiments at RT, and 1 sample in 2 areas at 120 K. The average dose for all positive and negative crossover at RT for the calibrated dose was 104 ± 14 MGy. The uncertainty is the standard deviation based on all Table 3 values and does not exclude outliers.

2.5. STXM analysis

Analysis of the electron beam exposed PFSA samples was carried out using STXMs at both the Advanced Light Source, beamline 5.3.2.2 (Warwick et al., 1998) and the ambient STXM on the Canadian Light Source beamline 10IDI (Kaznatcheev et al., 2007). Instrumentation (Kilcoyne et al., 2003) and data analysis (Hitchcock et al., 2012) have been described previously. Briefly, monochromated X-rays in the energy range of interest are focused onto the sample using a Fresnel zone plate (Centre for X-ray Optics, Berkeley, CA). The sample is raster-scanned perpendicular to the X-ray beam direction while detecting the transmitted X-ray intensity using a phosphor to down convert soft X-rays to visible light, which is then detected in single event counting mode using a photomultiplier tube. The position of the sample relative to the X-ray beam is actively controlled with few nm precision using differential interferometry (Kilcoyne et al., 2003). All samples were attached to standard trapezoidal aluminum support plates using epoxy or tape, loaded in the STXM chamber, which was then backfilled with He.

The transmitted intensity is converted to absorption (optical density, OD) through the Beer-Lambert law: $OD = ln(I_o/I)$, where I_o and I are the transmitted signals without and with the sample, respectively. The OD at each pixel is directly related to the sample properties through

$OD(E) = \mu(E) \cdot \rho \cdot h$, where μ(E) is the photon energy dependent mass-absorption coefficient, ρ is the density and h is the thickness of the material. All studies were performed using low dose STXM procedures in which the incident photon flux was decreased and the spot size was increased, with identical step and spot size (Melo, 2018). Images and image sequences (also called stacks (Jacobsen et al., 2000)) were acquired at the C 1s, O 1s and F 1s edges. In order to minimize additional radiation damage from the STXM stack measurements, the 30 nm full focus beam was intentionally defocused to 200 nm and a pixel spacing of 200 nm was used. Images were acquired at 280, 292.4, 320, 680, 690, and 710 eV, using 100 nm defocused beam and 100 nm pixel size. At each edge, the pre-edge images (i.e. 280 and 680 eV) were subtracted from the corresponding above-edge images in order to quantify radiation damage induced changes in the integrity of the C-F local environment. The intense 1 s → $\sigma^*_{C\text{-}F}$ peaks at 292.4 and 690 eV (Yan et al., 2018) decrease in intensity as the local structure changes due to radiation damage. In addition, after subtracting an extrapolation of the pre-edge signal from the full stacks, the NEXAFS spectra of each pad were integrated from 320 – 280 eV (carbon) and 710 – 680 eV (fluorine) to evaluate elemental changes. Typical doses imparted for single images

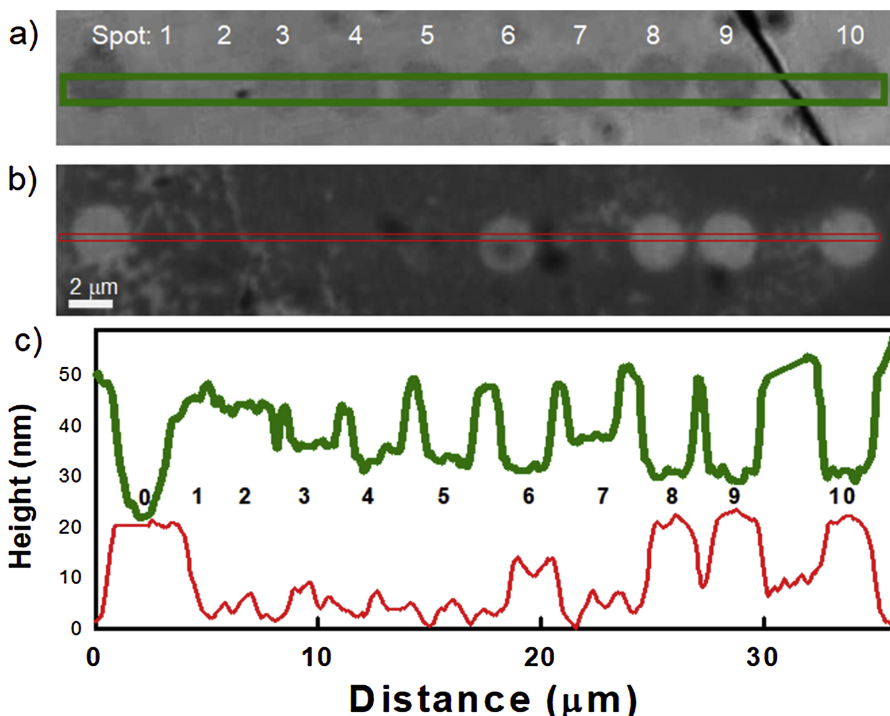

Fig. 1. Reflection mode bright-field optical microscopy images of a 50 nm thick polymethylmethacrylate (PMMA) film (sample set A, deposited on a 20 nm SiNx window, Table 2) damaged at RT with 200 kV electrons **(a)** before and **(b)** after lithographic development using a 5x objective lenses. **(c)** Line profiles of the thick (before; green in electronic version) and thin (after development, red in electronic version) areas used to calibrate the dose using the crossover from positive to negative mode. The thickness in the area of the undamaged sample was 50 nm (the value determined by STXM) and then a linear conversion of thickness to gray scale was assumed. The fluence for spots 1–10 are: 130, 310, 630, 940, 1250, 1880, (630), 2820, 3760, 7520 e^-/nm^2 corresponding to doses of 10, 24, 50, 74, 99, 149, (50), 223, 297, 594 MGy, using the conversion calibration 0.079 MGy/(e^-/nm^2). Spot 0 was a strongly damaged spot to provide an I_o for STXM measurements. Spot 7 was not correctly dosed. (For interpretation of the references to colour in this figure legend, the reader is referred to the web version of this article).

Table 3
Dose calculated from the measured fluence and the PMMA lithography cross-over calibration.

PMMA SAMPLE	Pad pre cross-link		Pad post cross-link		Cross-over calibrated dose (MGy)[b]
	Fluence ($\times 10^3$ e^-/nm^2)	Calibrated dose (MGy)[a]	Fluence ($\times 10^3$ e^-/nm^2)	Calibrated Dose (MGy)[a]	
A	1.25	96	1.88	145	121
A	0.94	72	1.76	136	104
A	0.87	67	1.63	126	96
A3	1.28	99	1.60	123	111
A3	1.28	99	1.91	147	123
A3	0.73	56	1.47	113	85
A3	1.19	92	1.48	114	103
A3	0.99	76	1.32	102	89
Average (std. dev.)	1.07 (0.21)	82 (16)	1.63 (0.21)	126 (16)	104 (14)
A2[c]	1.68	129	3.36	259	194
A2[c]	2.05	158	2.73	210	184

[a] Dose (MGy) = 0.079 ± 0.01 * Fluence (e^-/nm^2).
[b] Calculated from the dose for the pre and post-cross link areas, evaluated from the PMMA dose-fluence calibration (at RT).
[c] The relationship Dose (MGy) = 0.079 * fluence (e^-/nm^2) was used to convert the fluences for pre- and post-cross-over pads to dose for the cryo irradiated PMMA samples. This assumes that the fluence- dose relationship is independent of sample temperature and material, which is a reasonable assumtion since the radiation damage is generated by a wide range of inelastic scattering (20–500 eV) causing dissociative electronic excitation and ionization.

were less than 1 MGy while full stacks (images at > 100 energies) at multiple edges deposited less than 5 MGy (Melo, 2018).

X-ray damage (Melo, 2018; Melo and Hitchcook, 2018b) was studied using PFSA samples prepared on SiNx windows (5 x 5 mm, 200 µm frame, 1 x 1 mm 50 nm thick window, Norcada). X-ray damage was created in the STXM using an incident photon energy of 320 eV. This continuum energy was selected since all carbon atoms in the sample absorb at this energy, and since the spectral response of all species at this energy is broad and thus small errors in the energy scale calibration are not important. Patterns in a 3 × 3, 9 pad square array were irradiated with each pad having 10 × 10 exposure points and pixel spacings of 60, 120 or 180 nm. The X-ray beam was defocused by changing the distance between the ZP and sample so that the spot size was the same as the pixel spacing, and thus the full area of the pad was illuminated without overlap (Melo, 2018).

3. Results

3.1. PMMA exposure and cross-over dose at cryo temperatures

A PMMA film on SiNx mounted in a cryo-holder was damaged with 200 kV electrons while cooled to 120 K (Sample set A2, Table 2). Optical images of this sample before and after development are shown in Fig. 2. At 120 K, the ~50 nm thick PMMA film could sustain exposures of up to a fluence of 1.18 × 10^4 e^-/nm^2 corresponding to a dose of 910 MGy, with no signs of forming a hole. At 120 K the crossover transition occurred at a fluence between 2.05 ± 0.3 × 10^3 and 2.79 ± 0.4 × 10^3 e^-/nm^2. This is roughly double the fluence that caused the cross-over at RT (see Table 3) and corresponds to a dose of 184 MGy (based on the RT calibration of 0.079 MGy/(e^-/nm^2)). A second, independent evaluation placed the PMMA cross-over transition at 194 MGy. A doubling of the cross over exposure implies that at 120 K the sample must absorb twice

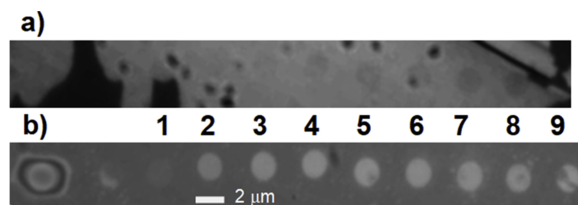

Fig. 2. Images of a 50 nm PMMA film deposited on a 20 nm SiNx substrate and damaged at cryo temperature (120 K). Optical images (a) before and (b) after development. The electron fluence (e^-/nm^2) for the spots numbered 1–9 was 840, 1680, 3360, 5040, 6710, 8400, 10100, 11800 and 4200. The black material at the left of the image of the undeveloped film is adventitious material that disappeared after the chemical development.

the energy to create the same degree of cross-linking damage (after sample warming) as at RT. An interpretation of this surprising result and comparison to related results from the literature is given in the Discussion.

3.2. NEXAFS spectra of undamaged versus electron damaged PFSA in cryo temperature

An area of a ~100 nm thick perfluorosulfonic acid (PFSA) film (Sample set B, Table 2) was damaged using 200 kV electrons with the

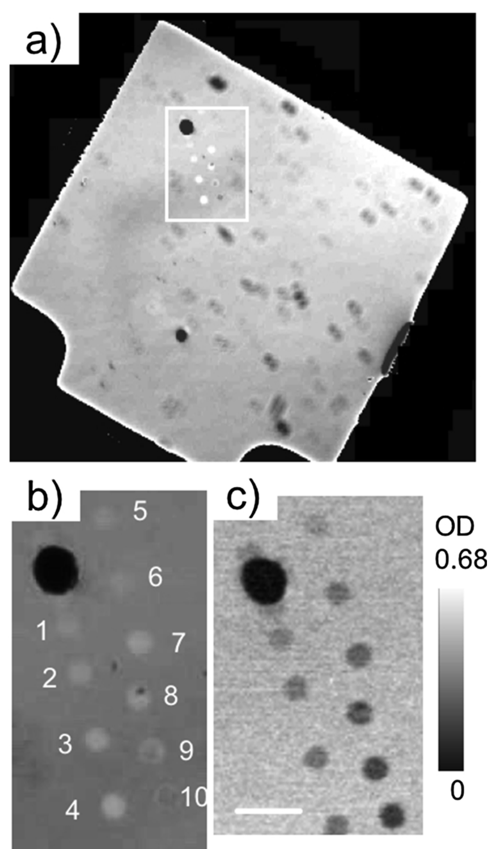

Fig. 3. Images of a 110 nm thick perfluorosulfonic acid (PFSA) film (sample set B, Table 2) free-standing on a Cu TEM grid, after damage with 200 kV electrons at 100 K. **(a)** Optical microscopy (5x magnification, reflection mode). The bright Cu grid areas have been masked out. **(b)** Optical microscopy (50x magnification, reflection mode) of the area indicated by the white rectangle in (a). **(c)** STXM OD image recorded at 690 eV. Scale bar is 5 μm. Spots numbered from 1 to 10 in (b), correspond to fluences of 330, 550, 770, 1100, 220, 550, 1100, 1530, 2200, 3280 e^-/nm^2, and electron beam doses: 26, 43, 61, 87, 17, 43, 87, 121, 174, 259 (MGy), using the conversion calibration 0.079 MGy/(e^-/nm^2). The dark black damaged spot was used to help locate the damaged region.

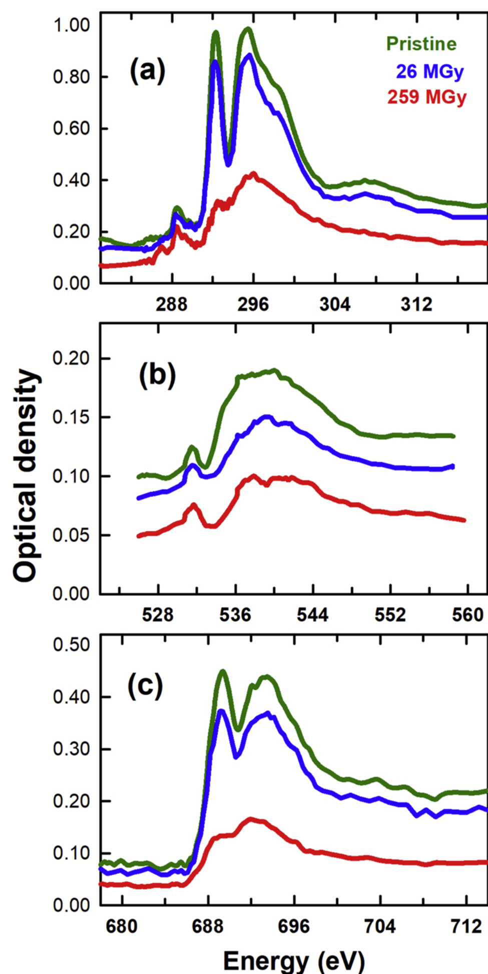

Fig. 4. NEXAFS spectra of a PFSA film (sample set B) recorded in STXM. **(a)** C 1s, **(b)** O 1s and **(c)** F 1s edges of a pristine area (green in electronic version, thick in print version), dose of 26 MGy (blue in electronic version, dashed in print version) and dose of 259 MGy (red in electronic version, thin in print version), damaged by 200 kV electrons in a TEM. (For interpretation of the references to colour in this figure legend, the reader is referred to the web version of this article).

sample cooled to 100 K. Fig. 3 shows post-damage images using optical microscopy (Fig. 3a, b) and a STXM OD image measured at 690 eV (Fig. 3c). All damaged regions are clearly visible in the optical microscopy image. As the dose increases, the OD in each damage spot decreases due to reduction in the intensity of the 690 eV feature (corresponding to amorphization of the –CF_2-CF_2- structures) and sample thinning due to radiation damage by the incident electron beam.

The C 1s, O 1s and F 1s NEXAFS spectra of two of the spots of damaged PFSA (spot #1 with 26 MGy and spot #9 with 259 MGy dose, Fig. 3b) are shown in Fig. 4, in comparison to the spectra of an area without intentional exposure. The C 1s and F 1s spectra of the undamaged PFSA are dominated by peaks at 292.4, 296, 690 and 694 eV related to excitations of C1s and F 1s core electrons to ground-state-unoccupied σ^*_{C-F} (⊥) and σ^*_{C-F} (//) transitions (Yan et al., 2018). The O 1s signal is dominated by a broad feature between 535–545 eV related to O 1s → σ^*_{C-O} and O 1s → σ^*_{S-O} transitions (Urquhart et al., 1995; Yan et al., 2018). There are small peaks at 289 and 532 eV, which have been attributed to C 1s → $\pi^*_{C=O}$ and O 1s → $\pi^*_{C=O}$ transitions at carboxylic/carboxylate groups terminating the PFSA chains (Yan et al., 2018).

Electron beam damage to PFSA results in extensive chemical changes and fluorine mass loss. At the C 1s edge (Fig. 4a), there is significant reduction in the intensity of the 292.4 eV and 296.2 eV

peaks. After 259 MGy, the 294–302 eV region of the C 1s spectrum of PFSA converts to a broad peak centered at 296 eV and the broad feature at 308 eV, attributed to C 1s → $\sigma^*_{C\text{-}C}$ transitions (Yan et al., 2018), disappears. New peaks associated with C 1s → $\pi^*_{C=C}$ and C 1s → $\pi^*_{C=O}$ transitions (Urquhart and Ade, 2002) are visible at 285.1 and 286.8 eV. There is a significant decay of the intensity in the pre-edge region of the C 1s spectra, which is dominated by the fluorine valence ionization continuum. This pre-edge decrease indicates extensive fluorine mass loss. The significant post-edge decay indicates carbon loss. At the O 1s edge (Fig. 4b), there is extensive decay in intensity over the full spectrum, including the pre-O1s edge. There is no significant evidence for oxygen mass loss since the pre-edge signal and post-edge O 1s signals change by similar amounts. Changes at the F 1s edge (Fig. 4c) are similar to those occurring at the C 1s edge with the F 1s → $\sigma^*_{C\text{-}F}$ (⊥) and F 1s → $\sigma^*_{C\text{-}F}$ (//) transitions at 690 and 694 eV decreasing as the dose increases. By a dose of 259 MGy, the peak at 690 eV has nearly disappeared and the double peaked structure has changed to a broad peak with a low energy shoulder. This damage is consistent with disordering, or amorphization, of the CF_2-CF_2 structure. The radiation damage transforms the distinct $\sigma^*_{C\text{-}F}$ (⊥) and $\sigma^*_{C\text{-}F}$ (//) electronic states into a broad band. The decrease in the F 1s continuum signal indicates fluorine mass loss.

Electron irradiation to a dose of only 26 MGy (exposure of 330 e-/nm^2) also results in enough damage to cause visible chemical changes and fluorine mass loss to the PFSA. One can argue that PFSA will always be damaged in TEM due to an inevitable dose from low magnification navigation. Supplemental Figure S-3 compares the OD spectra at the C 1s, F 1s and O 1s edge of ‘pristine’ PFSA, where ‘pristine’ designates an area not intentionally dosed. The spectra presented in Fig. S-3 were measured in STXM under very low damage conditions (less than 5 MGy). The ‘X-ray pristine’ sample (set C, green) was never examined by TEM. The ‘cryo TEM pristine’ sample (set B, red) was from a region not intentionally exposed by the TEM at cryo temperature. Since the two samples were of different thickness, the ‘X-ray pristine’ spectra were scaled to match intensities of the ‘cryo TEM pristine’ in the far continuum. The C 1s and F 1s spectra for the ‘X-ray pristine’ and ‘cryo-TEM pristine’ samples are nearly identical, while the O 1s signal of the ‘cryo-TEM pristine’ sample is slightly more intense than that of the ‘X-ray pristine’ sample. It is possible that, as the sample was warmed to RT, it adsorbed residual oxygenated contaminants from the TEM sample chamber. Since the C 1s and F 1s spectra of the cryo TEM pristine region and the X-ray pristine sample are nearly identical, we conclude that any low magnification viewing did not result in chemical changes.

3.3. Quantitative analysis of electron damaged PFSA

The changes caused by electron irradiation were quantified in several ways. First the net OD decay at chemically specific energies ($OD_{292.4\ eV} - OD_{280\ eV}$, and $OD_{690\ eV} - OD_{684\ eV}$) was evaluated as a function of dose. The critical doses derived from these signals are presented in Table 4. Second, the elemental loss (or gain) amounts were obtained by background subtraction and integration of the C 1s, F 1s and O 1s spectra. The damage versus dose curves for the elemental changes are plotted in Fig. 5. Where possible, each radiation damage (dose) curve was fit to an exponential function which assumes the damage follows first order kinetics (Beetz and Jacobsen, 2003; Coffey et al., 2002; Leontowich et al., 2012; Wang et al., 2009b):

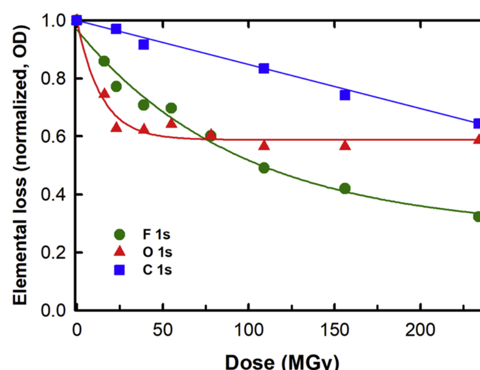

Fig. 5. Quantitative analysis of the changes in relative elemental amounts of F, C and O as a function of dose, derived from the F 1s, C 1s and O 1s STXM-NEXAFS spectra for PFSA (sample set B) under cryo conditions from the damage area shown in Fig. 4. The solid curves for the F-loss data, and for O-loss data below 50 MGy are fits to Eq. (3). That for C-loss is a linear fit.

$$OD = OD_\infty + b.\ \exp^{-D/a_c} \quad (3)$$

where OD_∞, b and a_c are fitting parameters, D is dose, and a_c is the critical dose. Recent investigations indicate that radiation damage (dose) curves like these can be fit with similar precision by several different mathematical models (Berejnov et al., 2018).

The a_c for fluorine loss for the cryo-TEM damaged PFSA derived from a fit of the data in Fig. 5 to Eq. (3) was 97 ± 17 MGy, with an OD_∞ = 0.3, which is the absorption for the remaining, radiation hardened, fluorine-depleted material. The carbon loss data could not be fit with an exponential decay model. Rather, it is fit by a linear decay, indicating zero-order kinetics. Initially the oxygen content decays rapidly. After 26 MGy, no further oxygen loss was observed. The a_c for oxygen loss derived from fitting the data from 0 to 50 MGy to Eq. (3) was 15 ± 3 MGy, with an OD_∞ = 0.6.

In order to understand the spectroscopic changes in terms of damage mechanisms and pathways, it is useful to examine how the intensities of specific transitions change as a function of increasing dose. STXM OD images of the same PFSA sample but electron irradiated areas different from those depicted in Fig. 3 (sample set B) were measured at specific transitions (285.1, 286.8, 292.4, 320 eV; 690.0, 710 eV) and in the C 1s (280 eV) and F 1s (684 eV) pre-edge region. Fig. 6(a–f) present differential STXM images (peak minus pre-edge), which isolates the

Table 4
Critical doses (MGy) for different damage processes in PFSA films damaged by 200 kV electron beam irradiation under different conditions.

Transition	Signal	a_c (MGy)				
		Sample				
		B (cryo)	I (cryo)	D (ambient)	E (SiNx)	F (SiNx + Pt)
C 1s → $\sigma^*_{C\text{-}F}$	$OD_{292.4\ eV} - OD_{280\ eV}$	117 ± 13	[a]	58 ± 15		
C 1s continuum	$OD_{320\ eV} - OD_{280\ eV}$	245 ± 13	[a]	[b]		
F 1s → $\sigma^*_{C\text{-}F}$	$OD_{690\ eV} - OD_{680\ eV}$	113 ± 13	96 ± 6	42 ± 15	87 ± 17	76 ± 9
F 1s continuum	$OD_{710\ eV} - OD_{680\ eV}$	101 ± 28	126 ± 36	[b]		
Elemental F	Integration of all the F 1s spectrum[c]	97 ± 17		42 ± 8		

[a] Values are not supplied for these evaluations due to saturation at the NEXAFS C 1s edge.
[b] Values are not supplied for these evaluations due to low signal to noise ratio.
[c] Background subtracted integrated spectra.

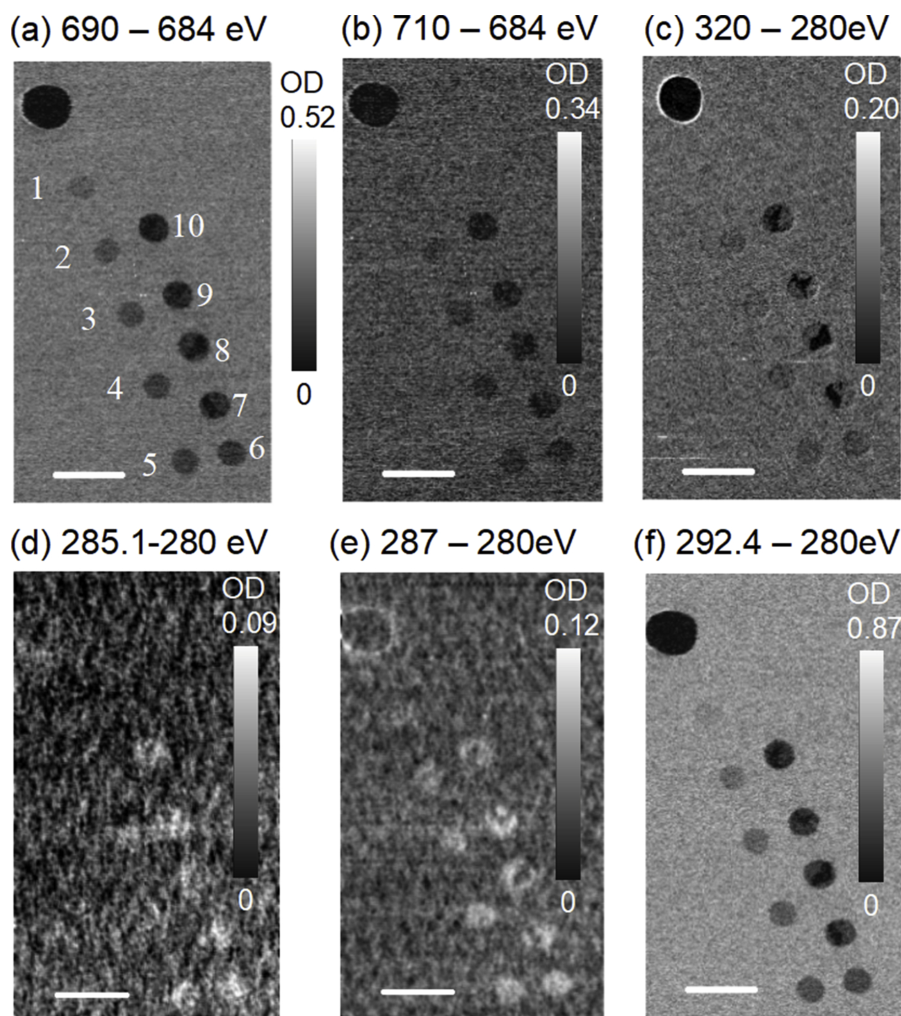

Fig. 6. STXM results for PFSA damaged under cryo conditions (Sample set B; different area from Fig. 2). **(a–f)** differences of OD images at the indicated photon energies in the F 1s and C 1s edges. The fluence used to generate spots 1–10 are: 220, 440, 660, 880, 1200, 1640, 2190, 2740, 3280, 4380 e^-/nm^2 corresponding to doses of 17, 35, 52, 70, 95, 130, 173, 216, 259, 346 MGy, using the conversion calibration 0.079 MGy/(e^-/nm^2). Scale bar is 5 µm.

changes only associated with the specific transition. The images at 292.4 and 690 eV, which are related to the degree of local –(CF_2-CF_2)– organization, have the highest contrast. The images at 285.1 eV and 286.8 eV, which arise from formation of new C=C and C=O bonds, have low contrast due to the weak signal (Fig. 4a). Fig. 7a plots the OD for each of the damage spots in Figs. 6(a–f) as a function of electron dose. This plot shows how the formation of C=O bonds, amorphization of C—F bonds, and elemental mass loss change as a function of electron dose.

3.4. Effect of temperature on electron damage to PFSA films

Fig. 7b plots the damage(dose) signals for CF_2-CF_2 amorphization ($OD_{690\ eV}$ - $OD_{680\ eV}$) while Fig. 7c plots damage(dose) signals for fluorine mass loss ($OD_{710\ eV}$ - $OD_{680\ eV}$), derived from TEM-induced damage to freestanding cryo-cooled and ambient PFSA films (sample set D). In each case the OD was divided by the OD for the undamaged material to compensate for thickness differences. The freestanding PFSA film (~60 nm thick as measured by STXM) ruptures after approximately 120 MGy which corresponds to ~1500 e^-/nm^2 when irradiated at RT. When irradiated at 100 K the film can sustain much more damage and does not rupture until the dose exceeds 460 MGy (over 5840 e^-/nm^2 on a ~100 nm film). The critical doses for CF_2-CF_2 amorphization and fluorine mass loss are similar to each other but are temperature dependent. The average of the values for CF_2-CF_2 amorphization and fluorine mass loss are 45 ± 7 MGy and 110 ± 10 MGy for RT and 100 K electron damaged PFSA, respectively. These results suggest that when the sample is cooled to 100 K, the film can sustain twice the dose as in the case of RT exposure when C—F structural disorganization and fluorine loss are evaluated by STXM.

3.5. Effect of silicon nitride support on electron damage to PFSA

Fig. 7b and c plots damage(dose) for electron beam damage to a freestanding PFSA film damaged at room and cryo temperatures, and for a RT damaged PFSA film deposited on a 100 nm SiNx window (sample set E, Table 2). Using a 100 nm SiNx substrate increases the critical doses for C—F amorphization and fluorine elemental mass loss by ~x2 compared to the values for a freestanding film (see Table 4) and also protects the film from rupturing when damaged at RT. At high doses (> 400 MGy), the normalized OD_∞ for analyzing $OD_{690\ eV}$ - $OD_{680\ eV}$ (dose) for the PFSA film on SiNx window is ~0.4 (Fig. 7b), which means that, after the damage effect saturates, the fluorine signal is ~40% of the original signal. This remaining fluorine material does not experience further changes up to doses > 500 MGy. The freestanding film ruptures at ~100 MGy before the OD reaches the OD_∞. For fluorine loss (Fig. 7c), the substrate affects the critical dose and the resulting damage(dose curve) does not follow an exponential model, indicating that the damage mechanism is different. The normalized OD_∞ for $OD_{710\ eV}$ - $OD_{680\ eV}$ is 0.6 for the film on SiNx. The higher

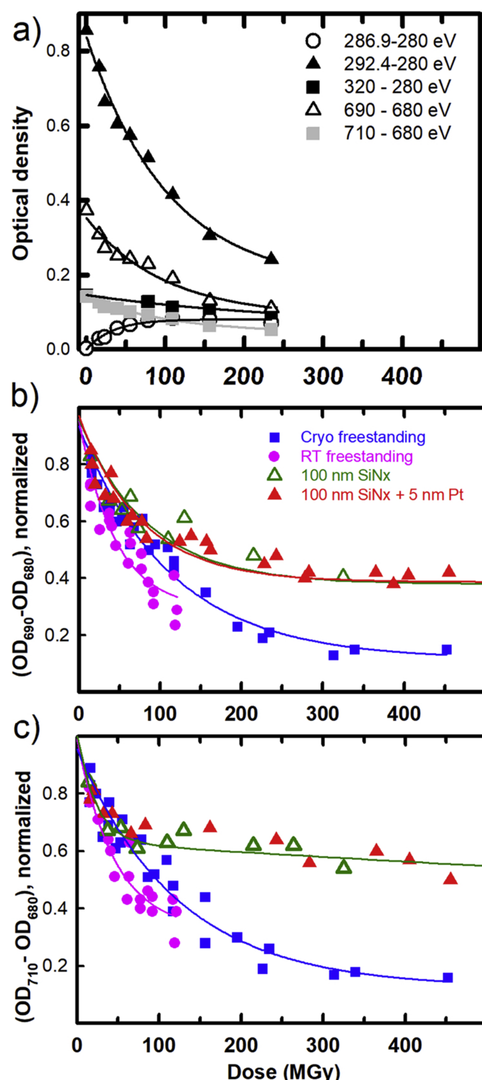

Fig. 7. OD decay as a function of dose for electron beam damage to PFSA. (**a**) derived from the indicated difference images from Fig. 6. (**b**) Change in $OD_{690\ eV} - OD_{680\ eV}$ (CF_2-CF_2 amorphization) as a function of dose for cryo (SiNx and free-standing) and room temperature (on SiN_x and SiN_x covered with 5 nm Pt). (**c**) Change in $OD_{710\ eV} - OD_{680\ eV}$ (F-loss) as a function of dose for cryo (SiNx and free-standing) and room temperature (on SiN_x and SiN_x covered with 5 nm Pt). For each data set exponential fits are also plotted. Quantitative critical dose results are presented in Table 4.

critical dose value for PFSA on a SiNx substrate than that for free-standing PFSA films indicates that the substrate prevents damage products diffusing out of the sample via the bottom surface.

3.6. Effect of Pt coating on electron damage to PFSA

An underlying 5 nm Pt coating, which was produced by electron beam sputtering Pt on the bare window, was examined to assess a possible role of substrate conductivity. Fig. 7b,c plot damage(dose) for 200 kV electron beam damage to a 50 nm PFSA film on a Pt-coated SiNx window (Sample set F, Table 2). Our results suggest that there was no significant effect of the Pt coating on the PFSA damage chemistry or critical dose measured by STXM. It is possible that the Pt coating on SiNx had a limited effect since the underlying SiNx was already providing adequate conductivity. Alternatively, it is possible that the sputtering process did not completely cover the surface and did not form a uniform layer capable of properly conducting the electrons.

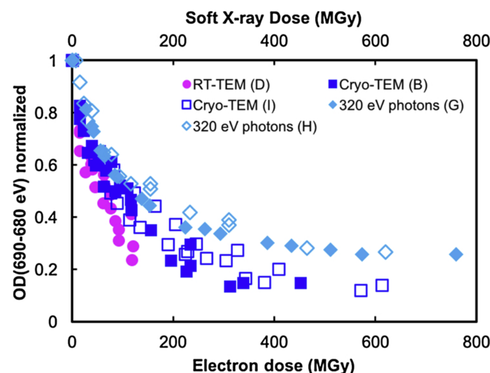

Fig. 8. Damage measured from the change $OD_{690\ eV} - OD_{680\ eV}$ (F 1s → $\sigma^*_{C\text{-}F}$ transition) as a function of dose for freestanding PFSA and PFSA on SiNx substrate damaged with electrons at RT (cyan triangles), freestanding at cryo temperature (blue, open and filled circles), and damaged with X-rays at RT (red, open and filled squares) (color in electronic version). For each curve, the sample set is indicated (see Table 1). Quantitative critical dose results are presented in Table 4. (For interpretation of the references to colour in this figure legend, the reader is referred to the web version of this article).

3.7. Quantitative comparison of electron and X-ray damaged PFSA

Fig. 8 compares damage(dose) curves for $OD_{690\ eV} - OD_{680\ eV}$ for PFSA films damaged by cryo and RT TEM to that for damage by soft X-ray irradiation at RT. PFSA films on SiNx substrate and freestanding PFSA films (sample sets G and H, respectively, Table 2) damaged by 320 eV photons have indistinguishable damage(dose) curves, indicating that the substrate does not play a role in the X-ray damage kinetics. The critical dose for -CF_2-CF_2- amorphization of PFSA is similar to that for freestanding PFSA films damaged by electrons at cryo temperature. The normalized OD_∞ values are 0.3 and 0.18, respectively. Between 0–100 MGy the normalized $OD_{690\ eV}$ - $OD_{680\ eV}$ signal is similar for all processes (cryo-TEM, RT-TEM, 320 eV X-rays), but the curves deviate at doses higher than 100 MGy (Fig. 8), with the electron beam damage continuing to increase while the X-ray damage stabilizes. It is possible that, for the continuous electron irradiation used to generate these pads, sample charging plays a role in the electron beam damage process after 100 MGy, resulting in more damage.

Fig. 9 is a bar chart comparison of the a_c critical doses measured for $OD_{690\ eV} - OD_{680\ eV}$ for 200 kV irradiated samples B, D, E, F and the RT X-ray irradiated sample. At RT, the a_c values for 200 kV electron beam induced CF_2-CF_2 amorphization for PFSA on SiNx (with, or without Pt) are roughly double that of the freestanding film. The ˜20% uncertainties

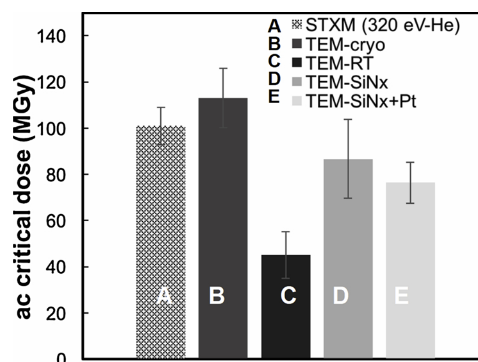

Fig. 9. Bar chart presentation of critical doses for 200 kV electron beam damage to PFSA evaluated from the intensity of the F 1s → $\sigma^*_{C\text{-}F}$ transition ($OD_{690\ eV} - OD_{680\ eV}$) as a function of dose for freestanding PFSA at room and cryo temperature and PFSA films on SiNx substrates. The critical dose for PFSA damage by 320 eV X-rays at RT is also indicated.

indicated in Fig. 8 are the standard deviation of 2–4 measurements in distinct areas of each sample.

4. Discussion

4.1. Critical evaluation of quantitation procedures

The value derived for converting exposure to dose using the PMMA lithography transition was 0.079(1) MGy/(e^-/nm^2). Egerton (2017, 2018) has used the equation

$$D(MGy) = (F)(E_{av} / IMFP)/\rho = (C/m^2)\ [E_{av}(eV)/IMFP(nm)]/\rho(g/cm^3) \quad (4)$$

to calculate a value of 0.037 MGy/(e^-/nm^2) for 100 keV electron irradiation of a 'typical organic solid' with the average energy loss per inelastic scattering event, also known as stopping power, $E_{av} \approx 42$ eV (including K-shell contributions), $\rho \approx 1.8$ g/cm^3 and an electron inelastic mean free path (IMFP) of 100 nm (Akar et al., 2006; Shinotsuka et al., 2015). In order to compare our experimentally derived value with that reported by Egerton (2018), we need to correct for the different electron energy used in this work (200 kV, which will have a longer mean free path and a lower E_{av}) and the lower density of PMMA (1.2 g/cm^3). According to Berger et al (2005), from 100 to 200 kV the stopping power (E_{av}) for carbon drops ~x2. According to Zhang et al. (2011) the mean free path increases by ~10% over the same interval. If we incorporate these factors, the expected conversion from fluence to dose for PMMA damaged at 200 kV is 0.025 MGy/(e^-/nm^2). If one uses the ESTAR E_{av} values (Berger et al., 2005), which are 105 eV and 70 eV for PFSA and PMMA, respectively, the dose/fluence ratio increases significantly to 0.084 MGy/(e^-/nm^2). Given the significant uncertainties in some of the parameters in Eq. (4), we think the level of agreement between Egerton's calculated value (corrected to 200 kV) and our experimental value is reasonable. One possible issue which we have not yet been able to explore but will do so in the near future, is the influence of the MWt of the PMMA polymer, which was only 120 kD, instead of 320 kD in the original work on dose calibration using the PMMA lithography transition (Leontowich et al., 2012). One might expect shorter chains to cross-link at lower dose since the active cross-linking agents should be more mobile in a shorter chain environment.

4.2. Chemical changes detected by NEXAFS: Electron versus X-ray damage to PFSA

A comparison of the C 1s and F 1s spectra of PFSA dosed with 20 MGy of 320 eV soft X-rays (Melo & Hitchcock 2018b) (not shown) and that dosed with 26 MGy of 200 kV electrons (Fig. 4) indicates that, for a similar dose, the spectra, and thus the chemical changes, are very similar. The similarity of the chemical changes caused by electron and X-ray irradiation suggests that most of the damage arises from secondary electrons generated after the initial ionization, as previously hypothesized (Wang et al., 2009a; Egerton, 2012). While the kinetic energy distributions of the primary electrons differ between electron and X-ray irradiation, with the X-ray case having more energetic photoelectron(s) from valence ionization, the energy in the primary particles is rapidly dissipated into a swarm of intermediate (5–20 eV) kinetic energy electrons that are still able to break bonds. Secondary electrons generated by both types of radiation result in further ionization, generating energetic electrons, ions and radicals, leading to a cascade of damage reactions. The electron beam induced changes are very similar to those observed in soft X-ray damaged PFSA (Melo and Hitchcook, 2018a, b). The a_c for –(CF_2-CF_2)- and fluorine loss for the cryo-TEM damaged PFSA (see Section 3.4) is similar to the values determined for 320 eV X-ray damage to PFSA at RT in a He environment (with residual O_2) (Melo and Hitchcook, 2018b). There are small differences in the F 1s pre-edge signal (compare Fig. 4c with Fig. 1c in Melo and Hitchcook, 2018b) which we interpret as due to carbon build-up in the STXM during the X-ray damage exposure. The vacuum in electron microscopes (10^{-5} Pa) is much better than that in the STXM chamber (~20 Pa). In addition, a cold finger used in the TEM minimizes carbon contamination. This is also consistent with the lower change in the quantity of elemental carbon in STXM damage (Melo, 2018; Melo and Hitchcook, 2018b) relative to TEM damage (this work).

With increasing dose, amorphization of the C—F bonds and fluorine loss occur with similar damage(dose) curves. The scission of the C—F bonds and subsequent chemistry results in the formation of volatile products. The most stable product is probably CF_4 from recombination of F- and CF_3- radicals, rather than F_2 (Forsythe and Hill, 2000). The fact that carbon loss is much smaller than fluorine loss at any given dose (see Fig. 5) seems consistent with formation of CF_3 or CF_4 molecules. Electron beam irradiation of a co-polymer of PTFE with ether bonds (i.e. polytetrafluoroethylene-co-perfluoropropyl vinyl ether with ether bonds, PFA) in vacuum resulted in formation of COF and COOH groups which were detected by infrared spectroscopy (Lappan et al., 2003).

According to Fig. 7, the critical doses for chemical damage for electron irradiated freestanding PFSA films are different from the values if the film is on a substrate. Fig. 8 shows that the substrate does not affect the critical doses for damage in X-ray irradiated PFSA. This qualitative difference might be due to sample charging, which is a larger with electron irradiation than X-ray irradiation.

4.3. Effect of sample temperature

Cooling samples to cryo temperatures when using electron or X-ray irradiation is known to reduce some, but not all, types of radiation damage (Beetz and Jacobsen, 2003; Egerton, 2013; Warkentin et al., 2013). For X-ray irradiation of PMMA, the critical dose for the O 1s(C=O) → $\pi^*_{C=O}$ transition with the sample at cryo temperature was the same as that with the sample at room temperature (Beetz and Jacobsen, 2003). However, oxygen loss was much lower when the loss was measured with the sample at cryo conditions rather than at room temperature (Beetz and Jacobsen, 2003). The reduced mass loss at cryo temperature is probably because the frozen material traps volatile damage products. This is apparently only a temporary measure since, after warming up, the sample showed a mass loss contrast similar to that for room temperature damage to the same sample with the same dose (Beetz and Jacobsen, 2003).

In this work, we found that the fluence at which the lithography cross-over transition occurred was approximately twice as large at 120 K than at RT, suggesting that the critical dose for cross-linking (formation of C=C bonds) of PMMA is higher under cryo conditions. An increase of the cross-over fluence (by 2–4 times) at cryo temperature (6–160 K) relative to room temperature was also observed by Gschrey et al. (2014) by measuring thickness changes with a profilometer of 200 nm thick PMMA films deposited on a clean GaAs:Si surface and damaged by a 10 kV electron beam in a scanning electron microscope (Gschrey et al., 2014). These authors speculated that, due to trapping of the gaseous radiation damage species, sample thinning was reduced at low temperatures (Gschrey et al., 2014).

Electron beam damage to samples at cryo temperatures will depend on the material (Lamvik, 1991). Electron irradiation damage quantification in the TEM is usually limited to elemental mass loss using EELS (Egerton, 1982, 2013; Yakovlev and Libera, 2006; Yakovlev et al., 2013). For PFSA damaged in a TEM, Yakolev & Libera (2006) used valence and core loss EELS to show that mass loss is reduced under cryo conditions. However, the difference was not quantified by these authors. If the damage products were only trapped at cryo temperature and then released when the film was warmed to RT, the extent of damage for a given dose would be similar for PMMA damaged at cryo then warmed to RT as that for the sample damaged in RT. Our observations suggest that the overall damage process is modified, perhaps because the volatile products trapped at cryo temperature can react to reform stable permanent bonds, either while cold, or when the sample is

warmed up to RT. This type of phenomena has previously been suggested for cryo-protection of soft materials (Group, 1986).

PFSA materials are known to contain pores in the nanometer range (Kusoglu and Weber, 2017; Mauritz and Moore, 2004). Ejecting the volatile fluorine containing damage products into the nanopores of PFSA might provide pathways for the damage product to escape, even at cryo temperature. If that was the case, then cooling PFSA would not affect the critical dose for damage in the same proportion as for PMMA, since the latter is non-porous. This situation may be different again in the case of damage to ionomer in PEM-FC electrodes where much larger and better connected pores exist.

4.4. Can TEM be used for direct visualization of the morphology of PFSA?

The dose-limited resolution (δ) for bright-field TEM imaging of organic materials such as PMMA has been estimated as 5 nm, assuming a signal to noise ratio (SNR) of 5 and a critical fluence of 630 e^{-}/nm^2 or 0.01 C/cm^2 (Egerton et al., 2012; Egerton, 2013). δ can be evaluated according to:

$$\delta = (SNR)(DQE)^{-0.5}C^{-1}\left(\frac{k\bullet F_c}{e}\right)^{-0.5} \quad (5)$$

where DQE is the detector quantum efficiency (estimated as 0.2 for electron counting detectors), C = 0.1 is the contrast between different resolution elements, k ˜0.8 is the efficiency of the signal-collection system, e is 1.6×10^{-19} C, and F_c is the critical fluence.

Since the radiation damage is small but already apparent at ~25 MGy (Fig. 4), we propose that 25 MGy should be the upper dose limit for meaningful quantitative studies of PFSA (Wu et al., 2018a). In TEM, 25 MGy corresponds to a fluence of ~300 e^{-}/nm^2 or 0.005 C/cm^2 which is ~1/4 of the critical dose when imaging PFSA in cryo conditions. The dose-limited spatial resolution for imaging PFSA with a dose of ~25 MGy calculated using the above parameters is 8 nm. This value decreases to 3.5 nm if a DQE of 1 is used (consistent with state-of-the-art direct electron detectors). This estimate indicates that only detectors with DQE of 1 have the potential to directly visualize the sub-5 nm hydrophilic and hydrophobic channels in PFSA, and even then, just barely. In addition, this work indicates that highest resolution TEM studies of PFSA should be performed at cryo temperatures using a substrate which protects the film from damage related to sample charging. At higher doses (> 300 e^{-}/nm^2 or 0.005 C/cm^2), even with the sample at cryo-temperature, radiation damage clearly changes the chemical structure of PFSA. The work presented in this manuscript calls into question the validity of conclusions drawn about the morphology of PFSA materials using TEM analyses with fluences greater than 300 e^{-}/nm^2. Yakovlev et al. (2013) concluded in their work that truly meaningful TEM imaging of PFSA (i.e. with the spatial resolution capable of visualizing individual hydrophilic domains) is not possible since images with high enough signal to noise ratio require an exposure that changes the morphology and results in elemental changes as seen with EELS. The results presented in this work directly corroborate Yakovlev's work. Studies using staining (Venkatesan et al., 2017; Lopez-Haro et al., 2014) may offer a route forward, although there is some concern that the staining may itself modify the material.

4.5. Recommendations for future studies of PFSA imaging

Analytical TEM measurements such as TEM-EELS and TEM-EDS require much larger doses. Thus, the dose-limited resolution for meaningful quantitative analytical measurements will be much larger than that for single images. A recent comparison of quantitative mapping of PFSA ionomer in PEM-FC cathodes by TEM-EDS and STXM-NEXAFS (Melo et al., 2017) exemplifies this point. Quantitative 2D maps of PFSA in catalyst layers can be achieved with STXM with negligible dose at ˜20 nm spatial resolution (Susac et al., 2011; Melo et al., 2017). The 3D distribution can also be measured by STXM but, due to the larger number of exposures needed, spatial resolution must be degraded [50 nm with negligible damage (Wu et al., 2018a)] or with significant damage despite achieving 15 nm using ptychography (Wu et al., 2018b). Recent improvements to soft X-ray ptychography (Shapiro et al., 2018) promise to significantly reduce the dose while achieving further improvements in spatial resolution.

Advances in electron microscopy instrumentation and development of new techniques have recently pushed the limits of low dose high resolution imaging of soft materials. For example, the use of pixelated detectors and ptychographic phase reconstruction offer “superior low dose performance for imaging weak phase contrast objects” (Yang et al., 2015). Using a non-convex Bayesian optimization to cryo-electron ptychography has been shown to reduce the required fluence for imaging biological samples (Pelz et al., 2017). Applying ptychography methods in TEM has allowed achieving record breaking spatial resolution, with reduced dose since a larger spot size is used (Wang et al., 2017; Jiang et al., 2018). It is possible that these recent developments can help achieve higher spatial resolution and thus overcome the limitations of TEM imaging PFSA due to radiation damage.

5. Summary

Electron irradiation at 120 K followed by warming to RT doubles the fluence for positive to negative cross-over for PMMA. Assuming the calibration of fluence and dose derived at RT holds at 120 K, our results indicate the dose needed for the lithography cross-over transition in PMMA and the critical dose for C–F amorphization and fluorine loss for PFSA is twice as large at 120 K relative to RT. The chemical changes to PFSA caused by electron and soft X-ray irradiation at RT are similar, and the critical doses for the same damage process are similar. This indicates that the damage processes for both types of radiation are dominated by damage caused by secondary electrons. A dose of 26 MGy, about 1/4 of the critical dose, is the recommended limit for TEM or X-ray measurements which will cause minimal changes to PFSA. At this dose (equal to a fluence of 330 e^{-}/nm^2), the dose limited resolution for bright field TEM imaging of PFSA is calculated to be 8 nm if the detector DQE = 0.2, or 3.5 nm if the detector DQE = 1. Our work questions the validity of conclusions drawn from previous literature on morphological/tomographic studies of PFSA materials using TEM imaging.

Acknowledgements

We thank Dr. Ray Egerton for helpful discussions about the fluence-dose conversion. Research supported by a Natural Sciences and Engineering Research Council (NSERC) Discovery grant and the CaRPE-FC network. TEM irradiation and imaging was performed using a JEOL 2010F TEM in the Canadian Centre for Electron Microscopy (CCEM) which is a national facility supported by the Canadian Foundation for Innovation under the MSI program, NSERC, and McMaster University. STXM measurements were performed using STXMs on beamline 5.3.2.2 at the Advanced Light Source (ALS) which is supported by the Division of Basic Energy Sciences of the U.S. Department of Energy under contract No. DE-AC02-05CH11231. Measurements were also made using the ambient STXM on beamline 10ID1 at the Canadian Light Source (CLS), which is supported by CFI, NSERC, CIHR, NRC and the University of Saskatchewan. We thank staff scientists, David Kilcoyne and Young-Sang Yu at ALS and Jian Wang at CLS for their assistance and support of the beamline and STXMs.

Appendix A. Supplementary data

Supplementary material related to this article can be found, in the online version, at doi:https://doi.org/10.1016/j.micron.2019.02.006.

References

Akar, A., Gümüş, H., Okumuşoğlu, N.T., 2006. Electron inelastic mean free path formula and CSDA-range calculation in biological compounds for low and intermediate energies. Appl. Radiat. Isot. 64, 543–550. https://doi.org/10.1016/j.apradiso.2005.11.014.

Allen, F.I., Comolli, L.R., Kusoglu, A., Modestino, M.A., Minor, A.M., Weber, A.Z., 2015. Morphology of hydrated As-cast nafion revealed through cryo electron tomography. ACS Macro Lett. 4, 1–5. https://doi.org/10.1021/mz500606h.

Bassim, N.D., De Gregorio, B.T., Kilcoyne, A.L.D., Scott, K., Chou, T., Wirick, S., Cody, G., Stroud, R.M., 2012. Minimizing damage during FIB sample preparation of soft materials. J. Microsc. 245, 288–301. https://doi.org/10.1111/j.1365-2818.2011.03570.x.

Bedolla, D.E., Mantuano, A., Pickler, A., Mota, C.L., Braz, D., Salata, C., Almeida, C.E., Birarda, G., Vaccari, L., Barroso, R.C., Gianoncelli, A., 2018. Effects of soft X-ray radiation damage on paraffin-embedded rat tissues supported on ultralene: a chemical perspective. J. Synchrotron Radiat. 25, 848–856. https://doi.org/10.1107/S1600577518003235.

Beetz, T., Jacobsen, C., 2003. Soft X-ray radiation-damage studies in PMMA using a cryo-STXM. J. Synchrotron Radiat. 10, 280–283.

Berejnov, V., Rubinstein, B., Melo, L.G.A., Hitchcock, A.P., 2018. First-principles X-ray absorption dose calculation for time-dependent mass and optical density. J. Synchrotron Radiat. 25, 833–847. https://doi.org/10.1107/S1600577518002655.

Berger, M.J., Coursey, J.S., Zucker, M.A., Chang, J., 2005. ESTAR, PSTAR, and ASTAR: Computer Programs for Calculating Stopping-Power and Range Tables for Electrons, Protons, and Helium Ions (version 1.2.3). Natl. Inst. Stand. Technol., Gaithersburg, MD. URL http://physics.nist.gov/Star (accessed 5.2.18).

Bernard, S., Benzerara, K., Beyssac, O., Brown, G.E., Stamm, L.G., Duringer, P., 2009. Ultrastructural and chemical study of modern and fossil sporoderms by Scanning Transmission X-ray Microscopy (STXM). Rev. Palaeobot. Palynol. 156, 248–261. https://doi.org/10.1016/j.revpalbo.2008.09.002.

Braun, A., Huggins, F.E., Shah, N., Chen, Y., Wirick, S., Mun, S.B., Jacobsen, C., Huffman, G.P., 2005. Advantages of soft X-ray absorption over TEM-EELS for solid carbon studies - A comparative study on diesel soot with EELS and NEXAFS. Carbon N. Y. 43, 117–124. https://doi.org/10.1016/j.carbon.2004.08.029.

Cody, G.D., Brandes, J., Jacobsen, C., Wirick, S., 2009. Soft X-ray induced chemical modification of polysaccharides in vascular plant cell walls. J. Electron Spectros. Relat. Phenomena 170, 57–64. https://doi.org/10.1016/j.elspec.2008.09.007.

Coffey, T., Urquhart, S.G., Ade, H., 2002. Characterization of the effects of soft X-ray irradiation on polymers. J. Electron Spectros. Relat. Phenomena 122, 65–78. https://doi.org/10.1016/S0368-2048(01)00342-5.

Cullen, D.A., Koestner, R., Kukreja, R.S., Liu, Z.Y., Minko, S., Trotsenko, O., Tokarev, A., Guetaz, L., Meyer, H.M., Parish, C.M., More, K.L., 2014. Imaging and microanalysis of thin ionomer layers by scanning transmission electron microscopy. J. Electrochem. Soc. 161, F1111–F1117. https://doi.org/10.1149/2.1091410jes.

Egerton, R.F., 1982. Organic mass loss at 100 K and 300 K. J. Microsc. 126, 95–100.

Egerton, R.F., 2012. Mechanisms of radiation damage in beam-sensitive specimens, for TEM accelerating voltages between 10 and 300 kV. Microsc. Res. Tech. 75, 1550–1556. https://doi.org/10.1002/jemt.22099.

Egerton, R.F., 2013. Control of radiation damage in the TEM. Ultramicroscopy 127, 100–108. https://doi.org/10.1016/j.ultramic.2012.07.006.

Egerton, R.F., 2017. Scattering delocalization and radiation damage in STEM-EELS. Ultramicroscopy 180, 115–124. https://doi.org/10.1016/j.ultramic.2017.02.007.

Egerton, R.F., 2018. Radiation Damage to Organic and Inorganic Specimens in the TEM. Submitted to this same issue of Micron. .

Egerton, R.F., Lazar, S., Libera, M., 2012. Delocalized radiation damage in polymers. Micron 43, 2–7. https://doi.org/10.1016/j.micron.2011.05.007.

Forsythe, J.S., Hill, D.J.T., 2000. Radiation chemistry of fluoropolymers. Prog. Polym. Sci. 25, 101–136. https://doi.org/10.1016/S0079-6700(00)00008-3.

Gianoncelli, A., Vaccari, L., Kourousias, G., Cassese, D., Bedolla, D.E., Kenig, S., Storici, P., Lazzarino, M., Kiskinova, M., 2015. Soft X-ray microscopy radiation damage on fixed cells investigated with synchrotron radiation FTIR microscopy. Sci. Rep. 5, 1–11. https://doi.org/10.1038/srep10250.

Group, I.E., 1986. Cryoprotection in electron microscopy. J. Microsc. 141, 385–391. https://doi.org/10.1111/j.1365-2818.1986.tb02731.x.

Gschrey, M., Schmidt, R., Kaganskiy, A., Rodt, S., Reitzenstein, S., 2014. Study of high-resolution electron-beam resists for applications in low-temperature lithography. J. Vac. Sci. Technol. B, Nanotechnol. Microelectron. Mater. Process. Meas. Phenom. 32, 061601. https://doi.org/10.1116/1.4896671.

Hitchcock, A.P., Dynes, J.J., Johansson, G., Wang, J., Botton, G., 2008. Comparison of NEXAFS microscopy and TEM-EELS for studies of soft matter. Micron 39, 741–748. https://doi.org/10.1016/j.micron.2007.09.008.

Hitchcock, A.P., 2012. Soft X-ray imaging and spectromicroscopy. In: In: Tendeloo, G.Van, Dyck, V.D., Pennycook, S.J. (Eds.), Handbook on Nanoscopy, vol. II. Wiley-VCH Verlag GmbH & Co. KGaA, pp. 745–791.

Jacobsen, C., Wirick, S., Flynn, G., Zimba, C., 2000. Soft x-ray spectroscopy from image sequences with sub-100 nm spatial resolution. J. Microsc. 197, 173–184.

Jiang, Y., Chen, Z., Han, Y., Deb, P., Gao, H., Xie, S., Purohit, P., Tate, M.W., Park, J., Gruner, S.M., Elser, V., Muller, D.A., 2018. Electron ptychography of 2D materials to deep sub-ångström resolution. Nature 559, 343–349. https://doi.org/10.1038/s41586-018-0298-5.

Kammeyer, J.K., Park, C., Pablo, J.De, Zerbetto, F., Patterson, J.P., Gianneschi, N.C., 2017. Directly Observing Micelle Fusion and Growth in Solution by Liquid- Cell Transmission Electron Microscopy. pp. 17140–17151. https://doi.org/10.1021/jacs.7b09060.

Kaznatcheev, K.V., Karunakaran, C., Lanke, U.D., Urquhart, S.G., Obst, M., Hitchcock, a.P., 2007. Soft X-ray spectromicroscopy beamline at the CLS: commissioning results. Nucl. Instrum. Methods Phys. Res. Sect. A Accel. Spectrometers, Detect. Assoc. Equip. 582, 96–99. https://doi.org/10.1016/j.nima.2007.08.083.

Kilcoyne, A.L.D., Tyliszczak, T., Steele, W.F., Fakra, S., Hitchcock, P., Franck, K., Anderson, E., Harteneck, B., Rightor, E.G., Mitchell, G.E., Hitchcock, A.P., Yang, L., Warwick, T., Ade, H., 2003. Interferometer-controlled scanning transmission X-ray microscopes at the advanced light source. J. Synchrotron Radiat. 10, 125–136. https://doi.org/10.1107/S0909049502017739.

Klein, R.J., Fischer, D.A., Lenhart, J.L., 2008. Systematic oxidation of polystyrene by ultraviolet-ozone, characterized by near-edge X-ray absorption fine structure and contact angle. Langmuir 24, 8187–8197. https://doi.org/10.1021/la800134u.

Kusoglu, A., Weber, A.Z., 2017. New insights into perfluorinated sulfonic-acid ionomers. Chem. Rev. 117, 987–1104. https://doi.org/10.1021/acs.chemrev.6b00159.

Lamvik, M.K., 1991. Radiation damage in dry and frozen hydrated organic material. J. Microsc. 161, 171–181. https://doi.org/10.1111/j.1365-2818.1991.tb03081.x.

Lappan, U., Geißler, U., Scheler, U., Lunkwitz, K., 2003. Identification of new chemical structures in poly(tetrafluoroethylene-co-perfluoropropyl vinyl ether) irradiated in vacuum at different temperatures. Radiat. Phys. Chem. 67, 447–451. https://doi.org/10.1016/S0969-806X(03)00083-5.

Leontowich, A., 2012. Tunable Focused X-rays for Patterning and Lithography. PhD Thesis. McMaster University.

Leontowich, A.F.G., 2013. Utility of the G value and the critical dose to soft X-ray radiation damage of polyacrylonitrile. Radiat. Phys. Chem. 90, 87–91. https://doi.org/10.1016/j.radphyschem.2013.04.018.

Leontowich, A.F.G., Hitchcock, A.P., Tyliszczak, T., Weigand, M., Wang, J., Karunakaran, C., 2012. Accurate dosimetry in scanning transmission X-ray microscopes via the cross-linking threshold dose of poly(methyl methacrylate). J. Synchrotron Radiat. 19, 976–987. https://doi.org/10.1107/S0909049512034486.

Leontowich, A.F.G., Hitchcock, A.P., Egerton, R.F., 2016. Radiation damage yields across the carbon 1s excitation edge. J. Electron Spectros. Relat. Phenomena 206, 58–64. https://doi.org/10.1016/j.elspec.2015.11.010.

Lopez-Haro, M., Guetaz, L., Printemps, T., Morin, A., Escribano, S., Jouneau, P.-H., Bayle-Guillemaud, P., Chandezon, F., Gebel, G., 2014. Three-dimensional analysis of Nafion layers in fuel cell electrodes. Nat. Commun. 5, 5229. https://www.nature.com/articles/ncomms6229.

Mauritz, K.A., Moore, R.B., 2004. State of understanding of Nafion. Chem. Rev. 104, 4535–4585. https://doi.org/10.1021/cr0207123.

Melo, L.G.A., 2018. Soft X-ray Spectromicroscopy of Radiation Damaged Perfluorosulfonic Acid. PhD Thesis. McMaster University.

Melo, L.G.A., Hitchcook, A.P., 2018a. Comparison of electron and X-ray microscopies for characterizing perfluorosulfonic acid ionomer for fuel cell applications. 19Th International Microscopy Congress. . http://abstracts.imc19.com/pdf/abstract_738.pdf.

Melo, L.G.A., Hitchcook, A.P., 2018b. Optimizing Soft X-ray spectromicroscopy for fuel cell studies: X-ray damage of ionomer. Microsc. Microanal. 24 (Suppl 2), 460–461. https://doi.org/10.1017/S1431927618014538.

Melo, L.G.A., Hitchcock, A.P., Berejnov, V., Susac, D., Stumper, J., Botton, G.A., 2016. Evaluating focused ion beam and ultramicrotome sample preparation for analytical microscopies of the cathode layer of a polymer electrolyte membrane fuel cell. J. Power Sources 312, 23–35. https://doi.org/10.1016/j.jpowsour.2016.02.019.

Melo, L.G.A., Hitchcock, A.P., Jankovic, J., Stumper, J., Susac, D., Berejnov, V., 2017. Quantitative mapping of ionomer in catalyst layers by electron and X-ray Spectromicroscopy. ECS Trans. 80, 275–282. https://doi.org/10.1149/08008.0275ecst.

Melo, L.G.A., Hitchcock, A.P., Susac, D., Stumper, J., Berejnov, V., 2018. Effect of UV radiation damage in air on polymer film thickness, studied by soft X-ray spectromicroscopy. Phys. Chem. Chem. Phys. 20, 16625–16640. https://doi.org/10.1039/C7CP08621K.

Migunov, V., Ryll, H., Zhuge, X., Simson, M., Strüder, L., Batenburg, K.J., Houben, L., Dunin-Borkowski, R.E., 2015. Rapid low dose electron tomography using a direct electron detection camera. Sci. Rep. 5, 1–5. https://doi.org/10.1038/srep14516.

Ovsyanko, M., Yucelen, E., Pechnikova, E., Falke, M., Chen, Q., Zaluzec, N.J., 2018. Soft matter X-ray microanalysis in the analytical electron microscope. Microsc. Microanal. 24 (Suppl 1), 776–777. https://doi.org/10.1017/S1431927618004373.

Pelz, P.M., Qiu, W.X., Bucker, R., Kassier, G., Miller, R.J.D., 2017. Low-dose cryo electron ptychrography via non-convex Bayesian optimization. Sci. Rep. 7, 9883. https://doi.org/10.1038/s41598-017-07488-y.

Peron, J., Mani, A., Zhao, X., Edwards, D., Adachi, M., Soboleva, T., Shi, Z., Xie, Z., Navessin, T., Holdcroft, S., 2010. Properties of Nafion® NR-211 membranes for PEMFCs. J. Memb. Sci. 356, 44–51. https://doi.org/10.1016/j.memsci.2010.03.025.

Rightor, E.G., Hitchcock, A.P., Ade, H., Leapman, R.D., Urquhart, S.G., Smith, A.P., Mitchell, G., Fischer, D., Shin, H.J., Warwick, T., 1997. Spectromicroscopy of poly (ethylene terephthalate): comparison of spectra and radiation damage rates in X-ray absorption and electron energy loss. J. Phys. Chem. B 101, 1950–1960. https://doi.org/10.1021/jp9622748.

Rodriguez, J.A., Eisenberg, D.S., Gonen, T., 2017. Taking the measure of MicroED. Curr. Opin. Struct. Biol. 46, 79–86. https://doi.org/10.1016/j.sbi.2017.06.004.

Shapiro, D.A., Celestre, R., Enders, B., Joseph, J., Krishnan, H., Marcus, M.A., Nowrouzi, K., Padmore, H., Park, J., Warwick, A., Yu, Y.-S., 2018. The COSMIC Imaging Beamline at the Advanced Light Source: a new facility for spectro-microscopy of nano-materials. Microsc. Microanal. 24, 8–10. https://doi.org/10.1017/S1431927618012485.

Shinotsuka, H., Tanuma, S., Powell, C.J., Penn, D.R., 2015. Calculations of electron inelastic mean free paths. X. Data for 41 elemental solids over the 50eV to 200keV range with the relativistic full Penn algorithm. Surf. Interface Anal. 47, 871–888.

https://doi.org/10.1002/sia.5789.
Susac, D., Berejnov, V., Hitchcock, A.P., Stumper, J., 2011. STXM Study of the Ionomer Distribution in the PEM Fuel Cell Catalyst Layers. ECS Transactions, pp. 629–635. https://doi.org/10.1149/1.3635596.
Urquhart, S.G., Ade, H., 2002. Trends in the carbonyl core (C 1S, O 1S) –& pi*c = o transition in the near-edge X-ray absorption fine structure spectra of organic molecules. J. Phys. Chem. B 106, 8531–8538. https://doi.org/10.1021/jp0255379.
Urquhart, S.G., Hitchcock, A.P., Priester, R.D., Rightor, E.G., 1995. Analysis of polyurethanes using core excitation spectroscopy. Part II: inner shell spectra of ether, urea and carbamate model compounds. J. Polym. Sci. Part B: Polym. Phys. 33, 1603–1620. https://doi.org/10.1002/polb.1995.090331105.
Venkatesan, S.V., Hannach, M.E., Holdscroft, S., Kjeang, E., 2017. Probing nanoscale membrane degradation in fuel cells through electron tomography. J. Membr. Sci. 539, 138–143. https://doi.org/10.1016/j.memsci.2017.05.073.
Wang, J., 2008. Radiation Chemistry by Soft X-ray Spectromicroscopy. PhD Thesis. McMaster University.
Wang, J., Botton, G., West, M., Hitchcock, A.P., 2009a. Quantitative evaluation of radiation damage to polyethylene terephthalate by soft X-rays and high-energy electrons. J. Phys. Chem. B 113https://doi.org/10.1021/jp808289e. 1869–76.
Wang, J., Morin, C., Li, L., Hitchcock, A.P., Scholl, A., Doran, A., 2009b. Radiation damage in soft X-ray microscopy. J. Electron Spectros. Relat. Phenomena 170, 25–36. https://doi.org/10.1016/j.elspec.2008.01.002.
Wang, C., Krishnan, V., Wu, D., Bledsoe, R., Paddison, S.J., Duscher, G., 2013. Evaluation of the microstructure of dry and hydrated perfluorosulfonic acid ionomers: microscopy and simulations. J. Mater. Chem. A 1, 938.
Wang, P., Zhang, F., Gao, S., Zhang, M., Kirkland, A.I., 2017. Electron ptychographic diffractive imaging of boron atoms in LaB_6 crystals. Sci. Rep. 7, 2857. https://www.nature.com/articles/s41598-017-02778-x.
Warkentin, M., Hopkins, J.B., Badeau, R., Mulichak, A.M., Keefe, L.J., Thorne, R.E., 2013. Global radiation damage: temperature dependence, time dependence and how to outrun it. J. Synchrotron Radiat. 20, 7–13. https://doi.org/10.1107/S0909049512048303.
Warwick, T., Franck, K., Kortright, J.B., Meigs, G., Moronne, M., Myneni, S., Rotenberg, E., Seal, S., Steele, W.F., Ade, H., Garcia, a., Cerasari, S., Denlinger, J., Hayakawa, S., Hitchcock, a.P., Tyliszczak, T., Kikuma, J., Rightor, E.G., Shin, H.-J., Tonner, B.P., 1998. A scanning transmission x-ray microscope for materials science spectromicroscopy at the advanced light source. Rev. Sci. Instrum. 69, 2964.
Wu, J., Melo, L.G.A., Zhu, X., West, M.M., Berejnov, V., Susac, D., Stumper, J., Hitchcock, A.P., 2018a. 4D imaging of polymer electrolyte membrane fuel cell catalyst layers by soft X-ray spectro-tomography. J. Power Sources 381, 72–83. https://doi.org/10.1016/j.jpowsour.2018.01.074.
Wu, J., Zhu, X., West, M.M., Tyliszczak, T., Shiu, H.W., Shapiro, D.A., Berejnov, V., Susac, D., Stumper, J., Hitchcock, A.P., 2018b. High resolution imaging of polymer electrolyte membrane fuel cell cathode layers by soft x-ray spectro-ptychography. J. Phys. Chem. C 122, 11709–11719. https://doi.org/10.1021/acs.jpcc.8b02933.
Yakovlev, S., Libera, M., 2006. Cryo-STEM EELS of nafion saturated with an organic solvent. Microsc. Microanal. 12, 996–997. https://doi.org/10.1017/S1431927606067997.
Yakovlev, S., Balsara, N.P., Downing, K.H., 2013. Insights on the study of nafion nanoscale morphology by transmission electron microscopy. Membranes (Basel) 3, 424–439. https://doi.org/10.3390/membranes3040424.
Yan, Z.B., Hayes, R., Melo, L.G.A., Goward, G.R., Hitchcock, A.P., 2018. X-ray absorption and solid-state NMR spectroscopy of fluorinated proton conducting polymers. J. Phys. Chem. C 122, 3233–3244. https://doi.org/10.1021/acs.jpcc.7b11592.
Yang, H., Pennycook, T.J., Nellist, P.D., 2015. Efficient phase contrast imaging in STEM using a pixelated detector. Part II: optimisation of imaging conditions. Ultramicroscopy 151, 232–239. https://doi.org/10.1016/j.ultramic.2014.10.013.
Zailer, I., Frost, J.E.F., Chabasseur-Molyneux, V., Ford, C.J.B., Pepper, M., 1996. Crosslinked PMMA as a high-resolution negative resist for electron beam lithography and applications for physics of low-dimensional structures. Semicond. Sci. Technol. 11, 1235–1238. https://doi.org/10.1088/0268-1242/11/8/021.
Zhang, X., Jacobsen, C., Lindaas, S., Williams, S., 1995. Exposure strategies for polymethyl methacrylate from in situ x-ray absorption near edge structure spectroscopy. J. Vac. Sci. Technol. B Microelectron. Nanom. Struct. 13, 1477. https://doi.org/10.1116/1.588175.
Zhang, H., Egerton, R.F., Malac, M., 2011. EELS investigation of the formulas for inelastic mean free path. Microsc. Microanal. 17 (S2), 1466. https://doi.org/10.1017/S1431927611008208.
Zubavichus, Y., Fuchs, O., Weinhardt, L., Heske, C., Umbach, E., Denlinger, J.D., Grunze, M., 2004. Soft X-ray-induced decomposition of amino acids: an XPS, mass spectrometry, and NEXAFS study. Radiat. Res. 161, 346–358. https://doi.org/10.1667/RR3114.1.